Electronic Supplementary Material (ESI) for Materials Horizons.
This journal is © The Royal Society of Chemistry 2023

SUPPLEMENTARY INFORMATION

Solid-state thermal rectification of bilayers by asymmetric elastic modulus

Junbyeong Lee,‡[a] Seokjae Cha,‡[a] Byung Ho Lee,‡[b] Agha Aamir Jan,[a] Kizhakkekara Rijin,[c] Jaehun Yang,[a] Moon Ki Kim*[a,b,d] and Seunghyun Baik*[a,b]

[a]School of Mechanical Engineering, Sungkyunkwan University, Suwon 16419, Republic of Korea.

[b]Center for Nanotubes and Nanostructured Composites, Sungkyunkwan University, Suwon 16419, Republic of Korea.

[c]Department of Energy Science, Sungkyunkwan University, Suwon 16419, Republic of Korea.

[d]Sungkyunkwan Advanced Institute of Nanotechnology (SAINT), Sungkyunkwan University, Suwon 16419, Republic of Korea.

‡These authors equally contributed to this work

*corresponding author

e-mail: **mkkim1212@skku, sbaik@skku.edu**

Supplementary Text 1. Numerical simulation of the Frenkel-Kontorova model.

The nonlinear dynamics of a chain of classical particles, with the harmonic nearest-neighbor interaction and periodic on-site substrate potential, can be described by the Frenkel-Kontorova (*FK*) model [1-5]. Figure 1a shows a one-dimensional model consisting of two nonlinear lattices. Each lattice has 50 particles connected by nearest-neighbor springs with different stiffnesses (φ_L and φ_R), where subscripts L and R designate left and right segments, respectively. The interface spring stiffness between the lattices is φ_{int}. The two ends of the chain are in contact with higher (θ_H) and lower temperature (θ_L) baths, where $\theta_H = \theta_0 + \Delta\theta/2$, $\theta_L = \theta_0 - \Delta\theta/2$, and θ_0 is the non-dimensional reference temperature.

The one-dimensional chain is described by the Hamiltonian of the *FK* model which is known to have normal heat conduction [1, 4].

$$H = \frac{1}{2}\sum\left(m\dot{x}_n^2 + \varphi(x_{n+1} - x_n - a_0)^2 + 2(1 - cosx_n)\right) \quad (1)$$

where x_n is the position vector of nth particle, a_0 is the lattice constant, and m is the mass of a particle. For simplicity, m and a_0 are set as 1 ($m = a_0 = 1$) [1]. Each term represents the kinetic energy, interaction potential energy, and substantial potential energy, respectively [1, 4].

The equations of motion are derived as follows [4-6] and solved using the Adams-Bashforth-Moulton predictor-corrector method of order 1 to 13 [7].

$$\ddot{x}_i = \varphi(-2x_i + x_{i+1} + x_{i-1}) - sinx_i \quad (2)$$

$$\ddot{x}_1 = \varphi(-2x_1 + x_2) - sinx_1 - \zeta_L\dot{x}_1 \quad (3)$$

$$\ddot{x}_{100} = \varphi(-2x_{100} + x_{99}) - sinx_{100} - \zeta_R\dot{x}_{100} \quad (4)$$

where $\zeta_L = \dot{x}_1^2/\theta_H - 1$ and $\zeta_R = \dot{x}_{100}^2/\theta_L - 1$ when the left and right ends are in contact with θ_H and θ_L baths, respectively. Similarly, $\zeta_L = \dot{x}_1^2/\theta_L - 1$ and $\zeta_R = \dot{x}_{100}^2/\theta_H - 1$ when the left and right ends are in contact with θ_L and θ_H baths, respectively.

The local heat flux J_n is then calculated using equation (5) [1].

$$J_n = \varphi\langle\dot{x}_n(x_n - x_{n-1})\rangle \quad (5)$$

where $\langle\rangle$ represents temporal average. The J_n values of all particles in each segment are averaged, and a greater average is determined to be the forward direction heat flow ($J_{forward}$, thick red arrow in Figure 1a), compared with the reverse direction heat flow ($J_{reverse}$). The $J_{forward}$ and $J_{reverse}$ are calculated under the identical $\Delta\theta$ and θ_0, resulting in $TR = (J_{forward} - J_{reverse})/ J_{reverse} \times 100$ (%). The numerical simulations are repeated 40 times by assigning different random initial conditions (10^{-7} to 10^{-5}) to $\dot{x}_1$ and $\dot{x}_{100}$. Each data point in Figure. 1b-d indicates an average value of 40 simulations.

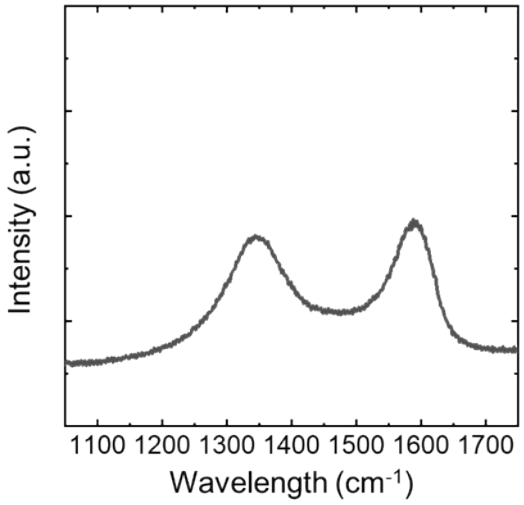

Figure S1. The characteristic Raman D and G modes of GO flakes.

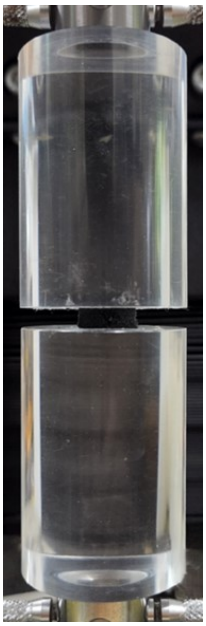

Figure S2. Experimental setup of the stress-strain measurements using a universal testing machine (crosshead speed = 2 mm min^{-1}).

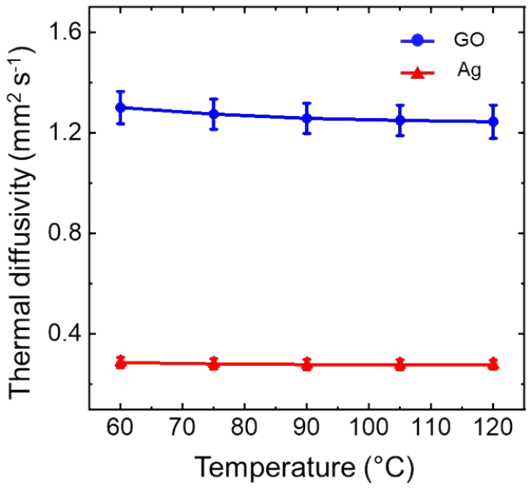

Figure S3. The thermal diffusivity of the GO and Ag layers measured by the laser flash method. The error bars represent the standard deviation of the data.

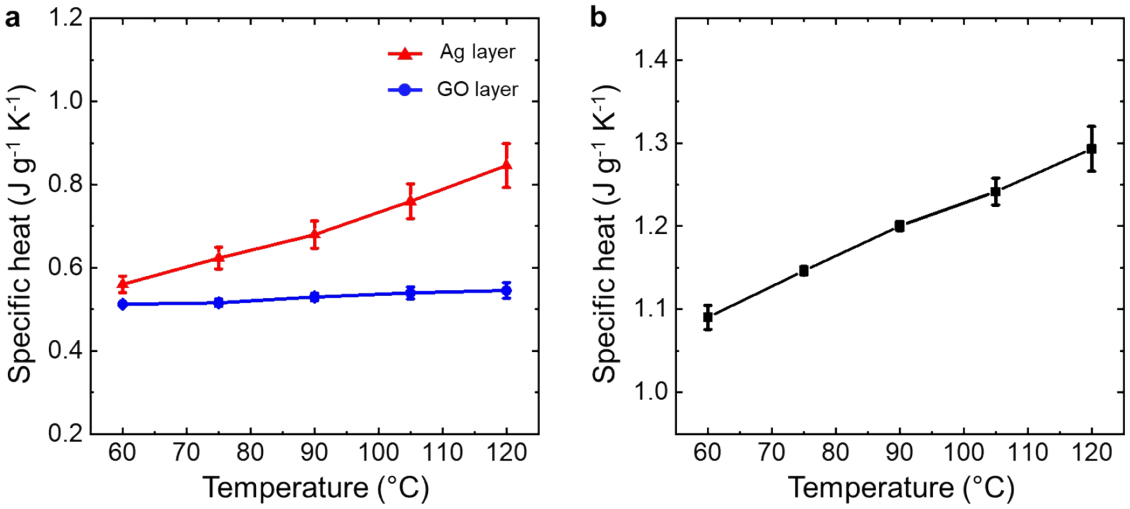

Figure S4. The specific heat measured by differential scanning calorimetry. a The Ag and GO layers of the Ag-GO specimen. The Ag particles are embedded in PDMS in the Ag layer. The increase in specific heat of the Ag layer with increasing temperature is primarily due to the PDMS polymer. **b** Pure PDMS polymer. The error bars represent the standard deviation of the data.

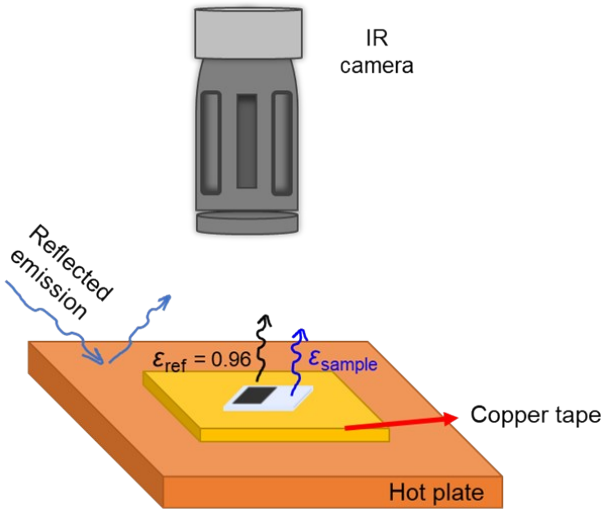

Figure S5. Schematic of the emissivity measurement setup. The reflected temperature and emissivity of the specimen are measured according to the ASTM standards [8, 9]. The black tape and specimen are placed on a copper tape, which is attached to the hot plate, and top surface temperatures are measured using an infrared (IR) camera.

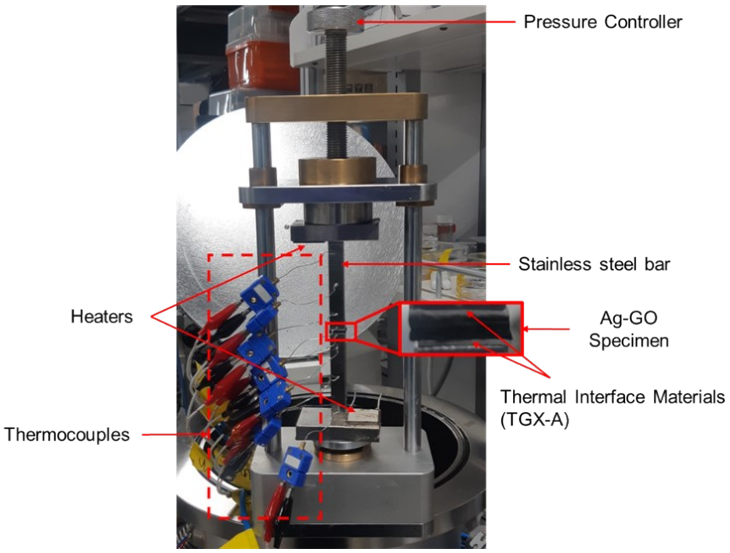

Figure S6. An optical image of the thermal rectification measurement setup. The specimen is installed between 2 stainless-steel heat conduit bars using thermal interface materials (TGX-A). The measurement is carried out in a vacuum chamber to avoid convection heat transfer.

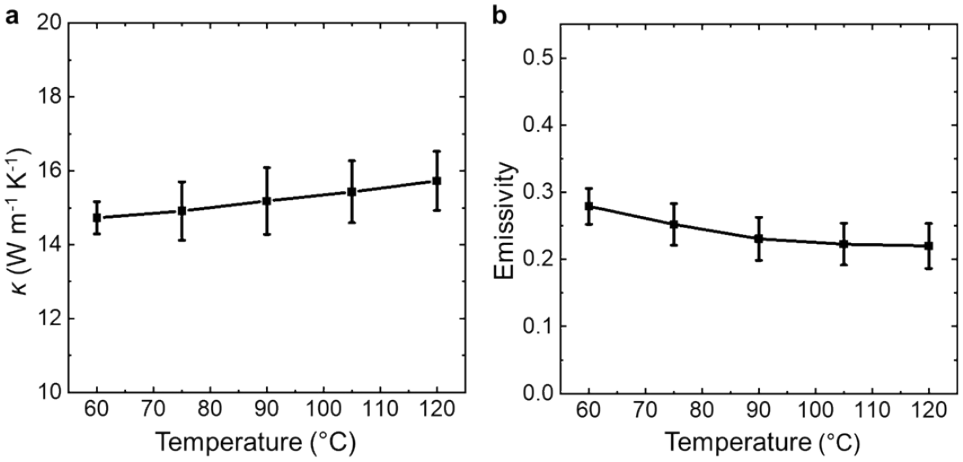

Figure S7. The temperature-dependent thermal properties of the stainless-steel bar. a Thermal conductivity. **b** Emissivity. The error bars represent the standard deviation of the data.

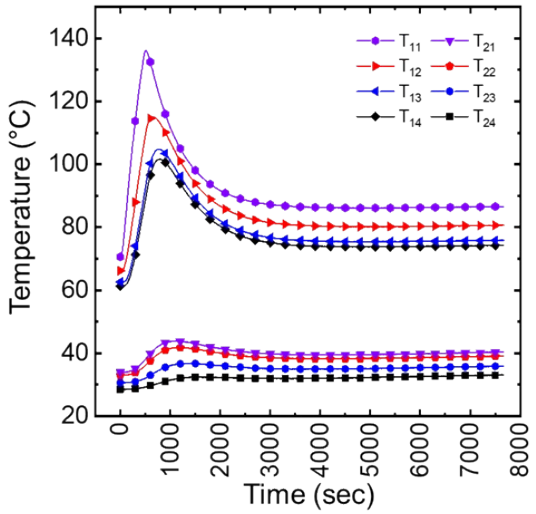

Figure S8. The temperature profiles of the stainless-steel bars as a function of time. A voltage, higher than the target voltage, is initially applied to shorten the time to reach a steady state. The target voltage (13 V) is then applied, and the steady state is reached after ~3600 seconds.

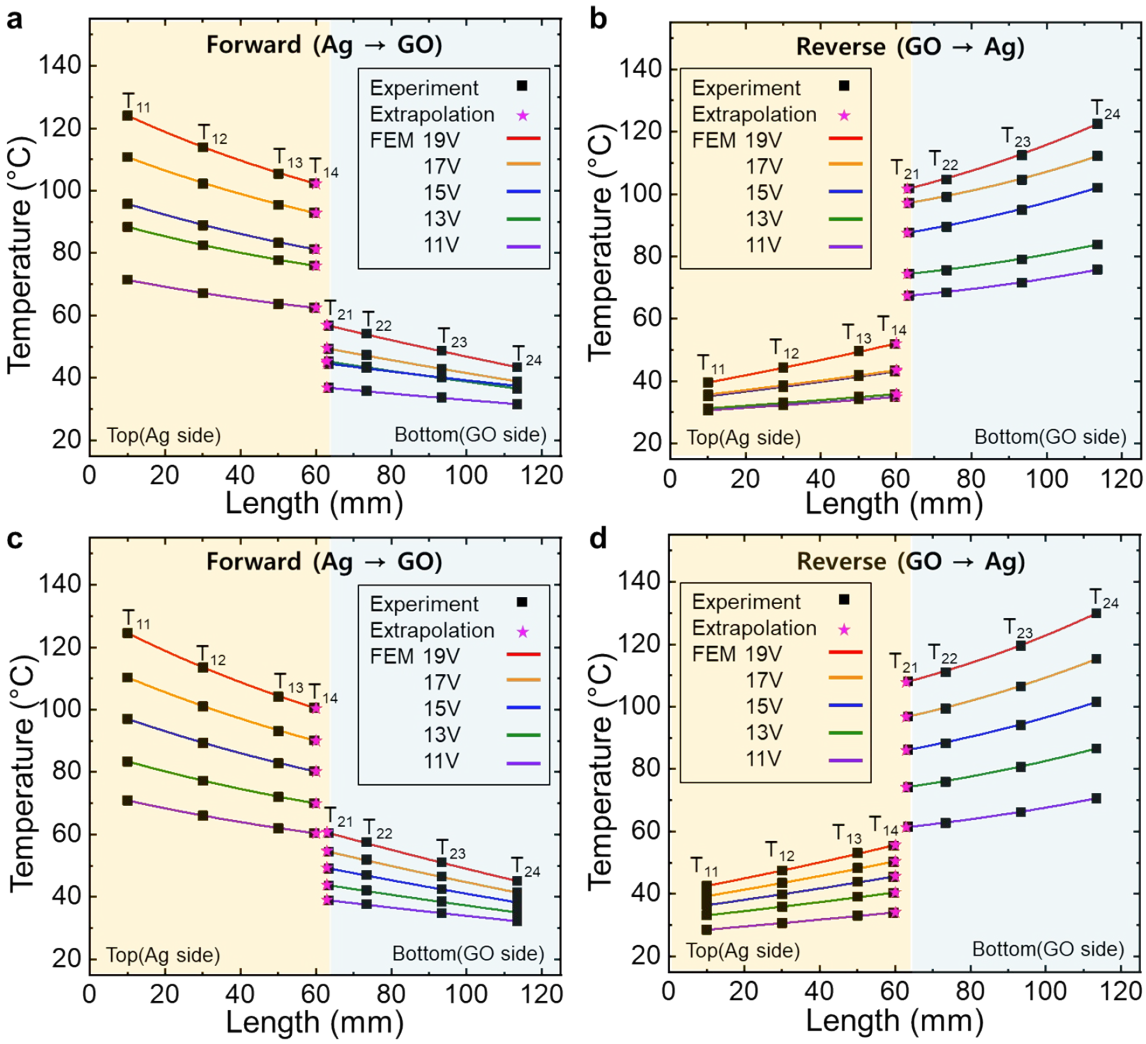

Figure S9. The comparison of the experimental data and FEM simulation results of the Ag-GO specimens. Three Ag-GO specimens are tested to demonstrate reproducibility. The experimental conditions are identical to those of the first specimen (Figure. 3b and 3c). **a, b** The second specimen data. **c, d** The third specimen data.

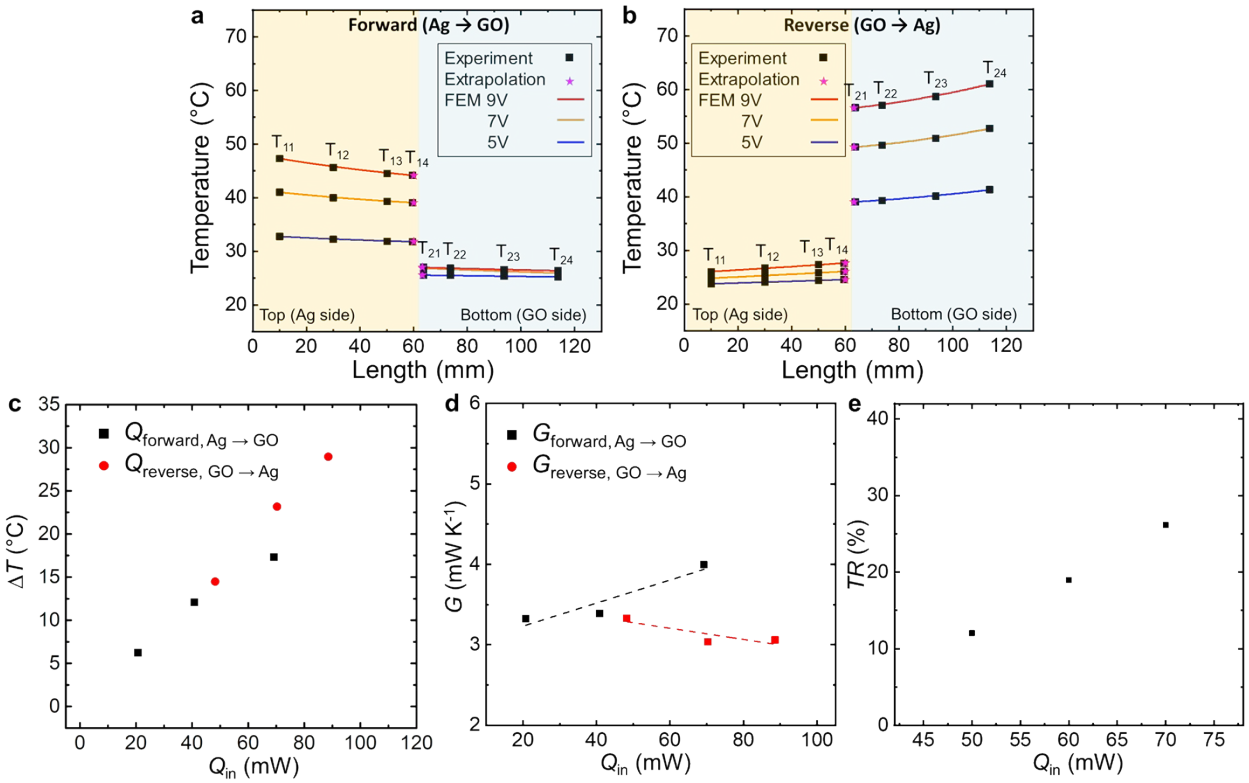

Figure S10. The thermal rectification of the Ag-GO specimen in a smaller Q_{in} range. a, b Experimentally measured temperature profiles in the forward and reverse heat flow directions. The applied heater voltage is changed between 5 and 9 V. The very end temperature of the stainless-steel bar is obtained by extrapolation using a second order fit. The FEM simulation results are also shown. **c** The forward and reverse direction temperature difference between two ends (ΔT) is shown as a function of Q_{in}. **d, e** The G and TR are shown as a function of Q_{in}.

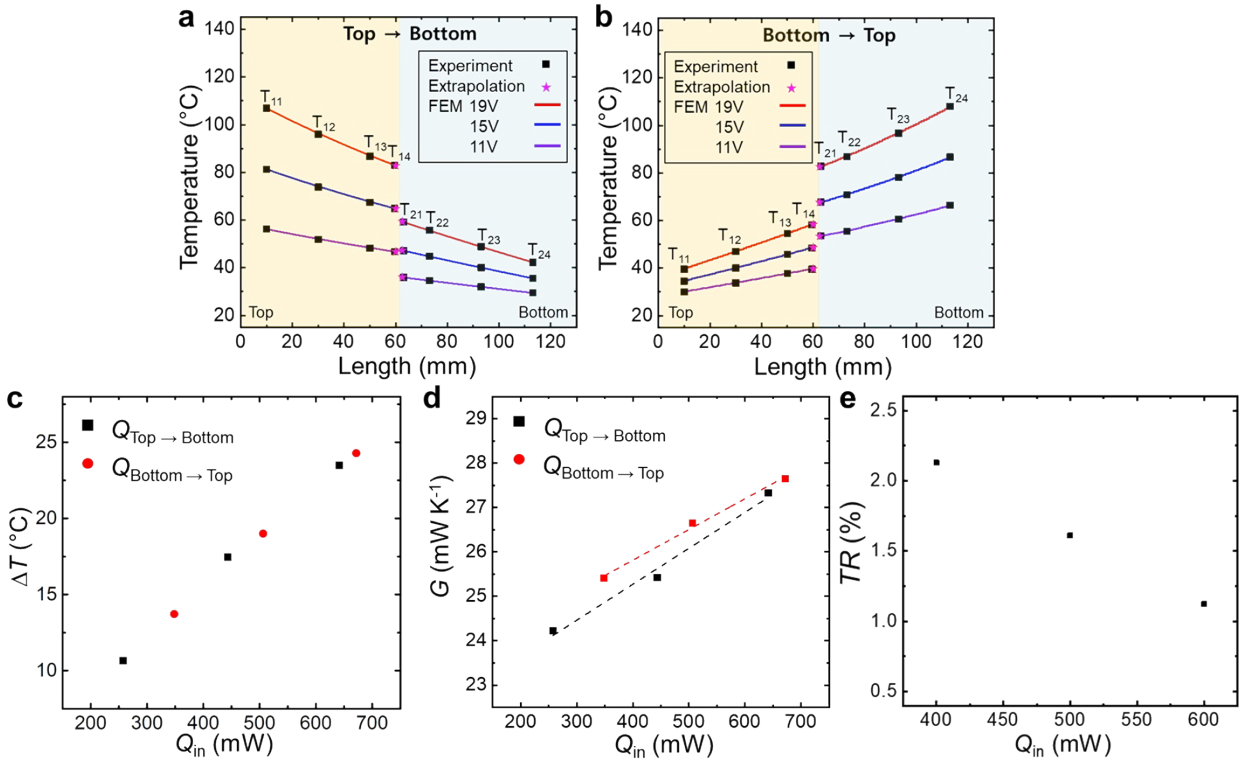

Figure S11. A uniform specimen prepared by coating the entire GO sponge with the Ag-PDMS solution. a, b Experimentally measured temperature profiles and FEM simulation results. The heat flow is firstly introduced from top to bottom, and then the direction is reversed. The applied voltages are 11, 15, and 19 V. **c** The temperature difference between two ends (ΔT) is shown as a function of Q_{in}. **d, e** The G and TR are shown as a function of Q_{in}.

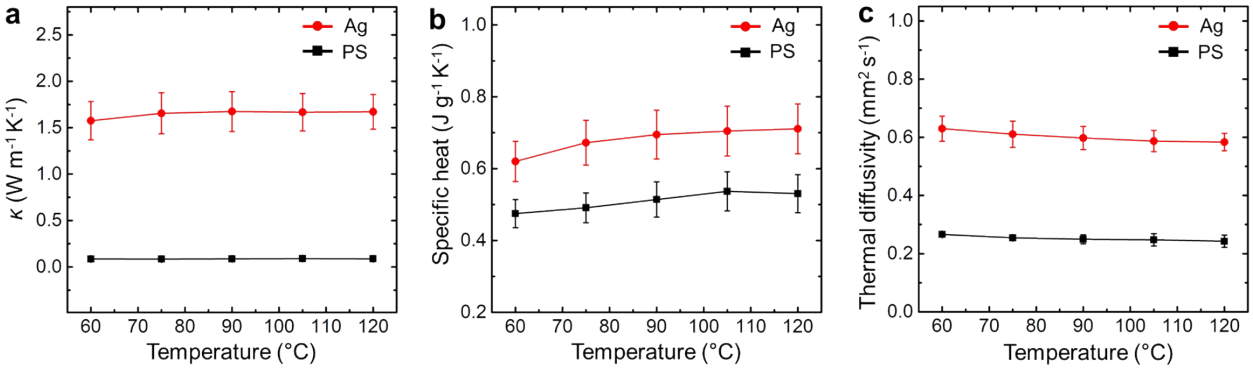

Figure S12. The thermal property of the Ag layer and harder PS layer of the Ag-PS specimen. Three specimens are tested at each condition. The error bars represent the standard deviation of the data. **a** Thermal conductivity. **b** Specific heat. **c** Thermal diffusivity.

Specimen	Layer	Electrical conductivity at 25 °C (S cm^{-1})
Ag-GO specimen	GO sponge	1.6×10^{-3}
	Ag layer	13
Ag-PS specimen	PS foam	~ 0
	Ag layer	936

Table S1. The electrical conductivity of each layer in the Ag-GO and Ag-PS specimens.

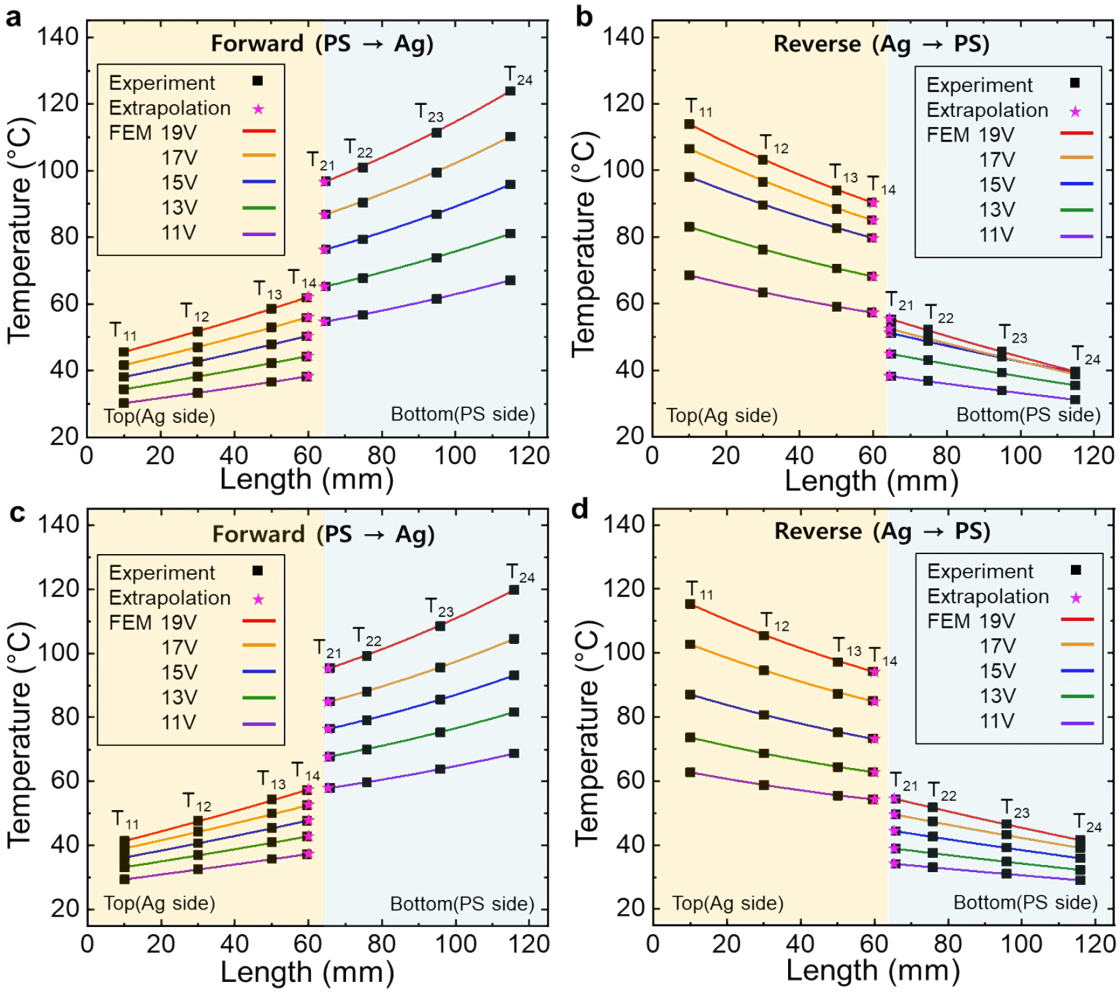

Figure S13. **The comparison of the experimental data and FEM simulation results of the Ag-PS specimens.** Three Ag-PS specimens are tested to demonstrate reproducibility. The experimental conditions are identical to those of the first specimen (Figure. 4b and 4c). **a, b** The second specimen data. **c, d** The third specimen data.

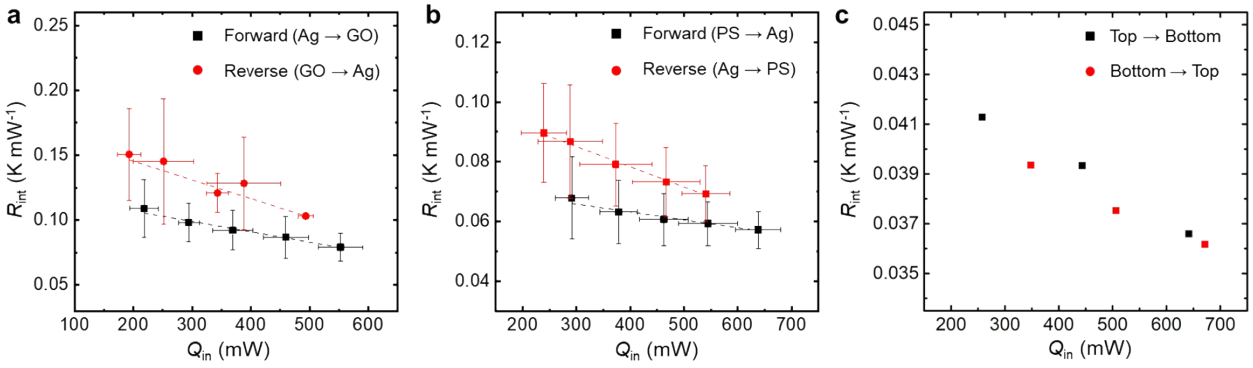

Figure S14. The interfacial thermal resistance between the stainless-steel bars calculated using the temperature profiles shown in Figures. 3b, 3c, 4b, 4c, S11a, and S11b. a The Ag-GO specimen. **b** The Ag-PS specimen. **c** The uniform specimen prepared by coating the entire GO sponge with the Ag-PDMS solution.

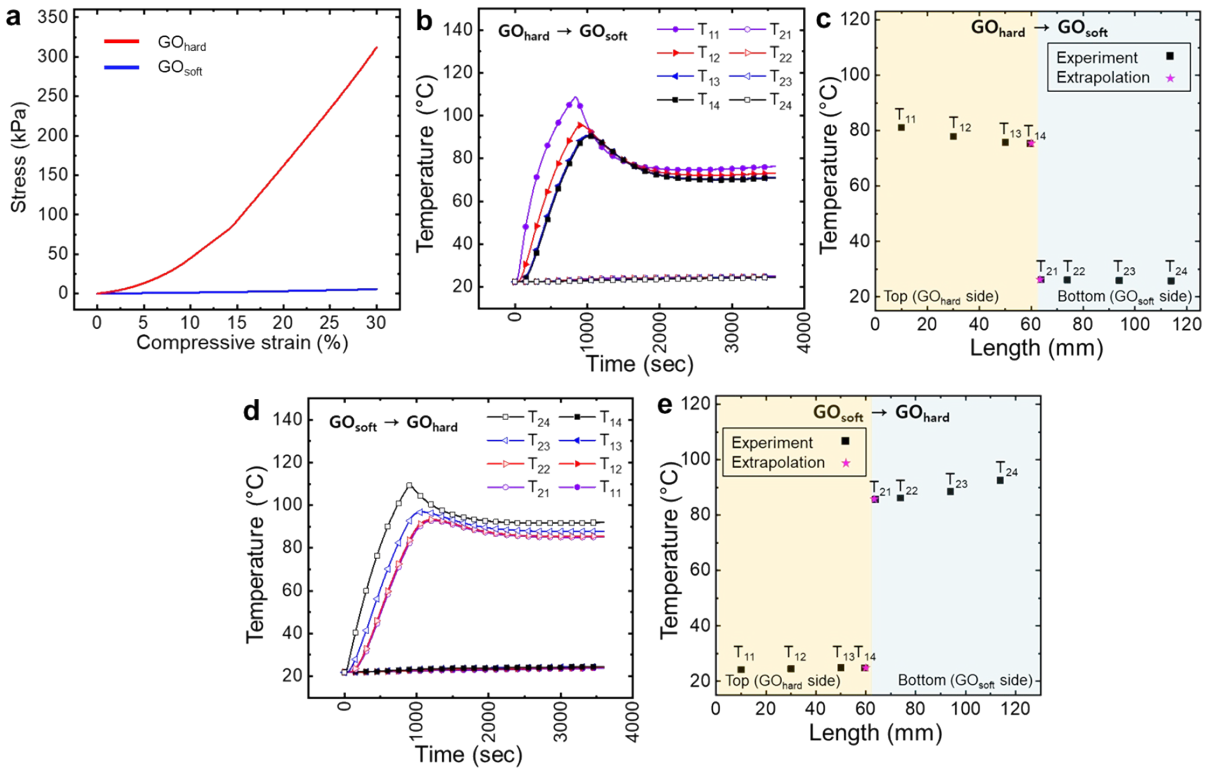

Figure S15. **A specimen consisting of the hard GO and soft GO parts is synthesized (10 mm × 10 mm × 2.9 mm) by filling the top half of the GO sponge with the PI polymer. a** The stress-strain characteristics. **b** The temperature profiles of the stainless-steel bars as a function of time. A voltage, higher than the target voltage, is initially applied to shorten the time to reach a steady state. The target voltage (15 V) is then applied to the top ceramic heater, and the steady state is reached at ~3600 seconds. **c** The steady state temperature profile ($GO_{hard} \rightarrow GO_{soft}$). **d** The temperature profiles of the stainless-steel bars as a function of time. The voltage is applied to the bottom ceramic heater (target voltage = 15 V). **e** The steady state temperature profile ($GO_{soft} \rightarrow GO_{hard}$).

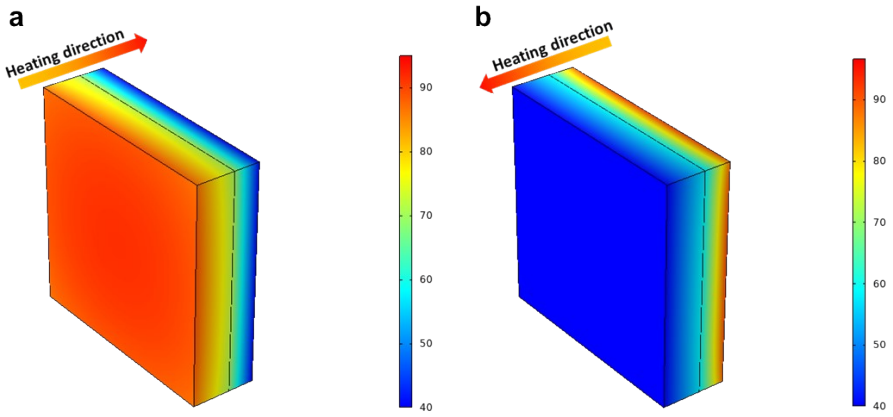

Figure S16. **The FEM simulation of the Ag-GO specimen.** The experimentally measured temperature-dependent κ and ε are used for the properties of each layer. The porous structure of the GO layer is not considered for simplicity. The convection heat transfer is not considered since the experiment is carried out in a vacuum chamber. A constant heat flow rate boundary condition is used (input heat flow rate = 294 mW, temperature of the sink side surface = 40 °C, surrounding temperature = 40 °C). The simulation is carried out by considering thermal conduction only (TR = 5.17%) or both conduction and radiation (TR = 7.77%). Note that the thermal rectification effect by elastic modulus asymmetry is not considered in the FEM simulation. Representative temperature profiles of the Ag-GO specimen are shown when both conduction and radiation are considered. **a** Forward heat flow. **b** Reverse heat flow.

Supplementary References

1. B. Li, L. Wang and G. Casati, *Physical Review Letters*, 2004, **93**, 184301.
2. B. Hu, L. Yang and Y. Zhang, *Physical Review Letters*, 2006, **97**, 124302.
3. M. Terraneo, M. Peyrard and G. Casati, *Physical Review Letters*, 2002, **88**, 094302.
4. O. M. Braun and Y. S. Kivshar, *Physics Reports*, 1998, **306**, 1-108.
5. B. Hu, B. Li and H. Zhao, *Physical Review E*, 1998, **57**, 2992-2995.
6. S. Lepri, R. Livi and A. Politi, *Physics Reports*, 2003, **377**, 1-80.
7. L. F. Shampine and M. W. Reichelt, *SIAM Journal on Scientific Computing*, 1997, **18**, 1-22.
8. *American Society for Testing and Materials International*, 2018.
9. *American Society for Testing and Materials International*, 2018.